PAPER

Growth kinetics and size-dependent wetting of Ag/α-Al_2O_3(0001) nanoparticles studied via the plasmonic response

To cite this article: Rémi Lazzari and Jacques Jupille 2012 *Nanotechnology* **23** 135707

Nanotechnology **23** (2012) 135707 (13pp) doi:10.1088/0957-4484/23/13/135707

Growth kinetics and size-dependent wetting of Ag/α-Al_2O_3(0001) nanoparticles studied via the plasmonic response

Rémi Lazzari and Jacques Jupille

[1] Institut des NanoSciences de Paris, Université Pierre et Marie Curie (Paris 6), CNRS UMR 7588, 4 Place Jussieu, 75252 Paris Cedex 05, France

E-mail: Remi.Lazzari@insp.jussieu.fr and Jacques.Jupille@insp.jussieu.fr

Received 1 February 2012, in final form 23 February 2012
Published 16 March 2012
Online at stacks.iop.org/Nano/23/135707

Abstract

The growth of vapour-deposited silver nanoparticles on α-Al_2O_3 was studied *in situ* from 190 to 675 K by surface differential reflectivity spectroscopy in the UV–visible range. Changes in size, shape and density were derived from the plasmonic response modelled in the framework of interface susceptibilities by assuming that supported clusters were in the form of truncated spheres. The sticking coefficient of silver on alumina is close to one up to $T \simeq 575$ K before entering a regime of incomplete condensation. The Arrhenius dependence of the saturation density indicates a nucleation on defects at low temperature ($T \leq 300$ K) and detrapping above. The particle size D evolution follows temporal power laws, independent of temperature and flux, which characterize the growth ($D \sim t^{0.31}$) and coalescence ($D \sim t^{0.55}$) of the film. These are indicative of the growth of isolated particles at constant density and dynamic coalescence, respectively. The wetting angle of the silver clusters is shown to increase during the growth regime, which is assigned to a combination of surface stress and mismatch-induced strain, and to decrease upon coalescence, which is attributed to plastic relaxation. For particles larger than 10 nm in size, the values of contact angle and adhesion energy level off with asymptotic limits ($\theta_c = 127.5° \pm 1°$ and 0.48 ± 0.02 J m^{-2}) that nicely agree with tabulated data. This work highlights the ability of nanoplasmics to monitor *in situ* the growth kinetics of thin supported films.

(Some figures may appear in colour only in the online journal)

1. Introduction

The non-wetting growth of particles from a vapour on a solid surface is often encountered in material science from dew formation or breath figures [1] to crystalline nanoparticle growth [2–5]. The issue concerns a wide variety of objects from liquids to crystalline particles of which the sizes range from nanometres to millimetres. Despite the enormous difference in length scales, Beysens *et al* [6] has already highlighted the existing similarities between metallic nanoparticles and macroscopic droplets of 1 μm to 1 mm in size that are easily probed by simple optical techniques [1, 7–10]. The comparison is all the more relevant for low adhesive, poorly matched metal/support interfaces and soft metals at high temperatures. For all objects that form upon condensation of an incoming flux on a substrate, the common emerging picture involves nucleation and growth in the influence area of the particles followed by coalescence when the particles merge upon contact [1, 2, 5, 7–9, 11–16]. Relationships that link the particle size D to the average thickness t of the film (or evaporation time) are derived from experiments, scaling arguments, analytical representations and numerical modelling. For the growth and the coalescence stages of three-dimensional (3D) particles supported on

two-dimensional (2D) surfaces, the scaling description of particles in the static approach leads to the power laws $D \sim t^{1/3}$ and $D \sim t$, respectively, that account for many observations [1, 6, 7, 11, 17].

The underlying assumption of static coalescence is that particles grow at fixed position and merge instantaneously compared to the growth time scale. This hypothesis is questionable in the light of numerous experimental [18–26] and theoretical [27–31] studies about particle diffusion with poorly matched and weakly bonded interfaces. The interplay with coalescence was explored by Steyer *et al* [32] in a simulation in which, at each step, the growing clusters underwent a random motion inversely proportional to the cluster size. Such a model was later associated with the so-called dynamic coalescence [2, 5]. At surface coverages between 0.01 and 0.2, Steyer *et al* found a bimodal size distribution with small particles growing by a diffusion-limited mechanism $D_{\text{small}} \sim t^{1/3}$. For larger clusters, however, the cluster size $D \sim t^{0.48}$ and density $\rho \sim t^{-0.45}$ escape the static picture. Similarly, for a mass conserved system, Brownian motion of particles modifies the time dependence of the average size; Meakin [9] found a $D \sim [t \ln(t)]^{1/3(1-\gamma)}$ behaviour assuming a particle diffusion coefficient which scales with its size as $D_{\text{F}} \sim D^{3\gamma}$. Although experimental studies of such phenomena are scarce, static coalescence was already questioned in the case of the growth of supported nanoparticles by (i) transmission electron microscopy studies (TEM) of liquid Sn on SiO_2 [33] with power laws $D \sim t^{0.86}$ and by (ii) grazing incidence small angle x-ray scattering [34] (GISAXS) studies of Pt/MgO(100) [35], Au/TiO_2(110) [36] and Ag/MgO(100) [37, 38], with $D \sim t^{0.5}$, $t^{0.54}$ and $t^{0.6}$, respectively. However, the shortcomings of the analyses limit the implications of these observations. TEM analysis relies on *ex situ* data with a limited number of points. GISAXS hardly explores the nucleation and growth stages and, because of the experimental burden, data collection is often restricted to unique temperature and flux [36, 35, 38]. Finally, the kinetics may not be analysed correctly since a GISAXS pattern is typically recorded within a few minutes [39, 34] at the surface coverages of concern.

Kinetic analysis of nanoparticle growth is far from being an easy task, in particular with real space imaging techniques which imply a time consuming point-by-point measurement [2–5, 40]. The purpose of this work is to take advantage of plasmonics to probe by light absorption the growth of a metal film in a wide temperature range and at different fluxes. It has been chosen to examine Ag/Al_2O_3(0001) by surface differential reflectivity spectroscopy (SDRS) in the UV–visible range. The system is characterized by an abrupt interface and the formation of interfacial oxide is unlikely with silver as expected from thermodynamics [3] and checked by *ab initio* modelling [41–44]. The quite weak adhesion should facilitate cluster diffusion. Silver films can be removed by desorption without perturbing the substrate which ensures a similar surface for all experiments. SDRS is of extreme relevance in analysing silver nanoparticles [45–48] for which it leads to morphology parameters that compare to those derived by grazing incidence small angle x-ray scattering (GISAXS) [37, 38]. In the same way as x-rays, light probes the size and density but also the shape. Both particle growth and adhesion (through wetting angle) are analysed simultaneously. In addition, the capability to record a spectrum within less than a second makes the technique much more flexible than GISAXS. We have recently developed a model specifically dedicated to the analysis of growth through plasmonic response [49]. Based on the determination of interface susceptibilities (IS), it accounts for temperature-dependent dielectric constants, finite-size effects, and homogeneous and heterogeneous broadening sources. Its physical relevance has been checked in the case of Ag/Al_2O_3(0001).

2. Experiments and results

2.1. Experimental setup

Experiments were performed in an ultra-high vacuum chamber (base pressure 3×10^{-8} Pa) equipped with all surface science facilities including x-ray photoelectron spectrometry (XPS), low energy electron diffraction (LEED) and surface differential reflectivity spectroscopy (SDRS) (see [48, 49] for all details). The Al_2O_3(0001) (10×10 mm^2, miscut lower than 0.5°) could be heated up to 1200 K and cooled down to 200 K. The sample temperature was measured with a chromel–alumel thermocouple firmly pressed on the substrate surface, with an uncertainty of 30 K estimated after calibration by melting metal pellets [49]. After cleaning by annealing at $T \simeq 1200$ K under an equivalent oxygen pressure of 10^{-4} Pa provided by a gas doser, the surface contamination of the alumina surface was below a per cent of a monolayer, as checked by XPS. A sharp LEED pattern and *ex situ* atomic force microscopy image confirmed the presence of large terraces (see figure 1 of [48]). Silver was evaporated from an effusion cell. The deposition rate ($F = 0.075$–0.3 nm min^{-1}) was calibrated with a quartz microbalance. Several growth temperatures were explored (190, 300, 425, 575, 675 K). The clean surface was restored by film desorption above 900 K so that all the films were grown on the same substrate. Some films were characterized *ex situ* by a Nanoscope III atomic force microscope that was run in tapping mode.

SDRS spectra correspond to the variation $\Delta\mathcal{R}/\mathcal{R}$ of the sample reflectivity with respect to the reflectivity of the bare surface during silver deposition at constant flux. The SDRS setup [39, 49] consisted of a deuterium lamp whose light was focused on the surface at an incident angle of $\theta_0 = 45°$ through silica windows. The optical range extended from 1.5 eV (wavelength $\lambda = 826$ nm) to 6 eV ($\lambda = 210$ nm) with a resolution of ~5 nm and a stability below 5×10^{-3}. The reflected light was polarized along the plane of incidence; in p-polarization, the electric field allows probing excitations along the two directions of space, parallel and perpendicular to the substrate. Light collected by a silica condenser into optical fibres was analysed on a spectrometer (Oriel-MS125) equipped with a 300 grooves mm^{-1} grating blazed at 300 nm to enhance the UV signal. The light was dispersed on a 14 bit Peltier cooled photodiode array (1024 pixels). As the film

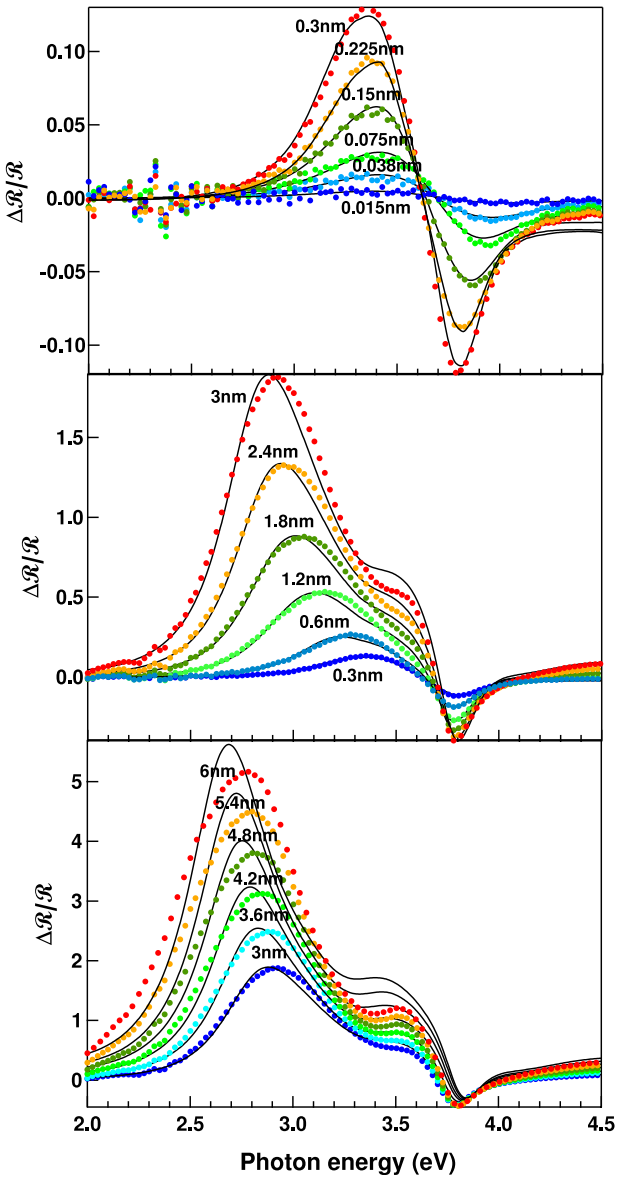

Figure 1. Evolution of the SDRS spectra during silver growth on $Al_2O_3(0001)$ at $T = 300$ K (growth rate 0.3 nm min^{-1}). The continuous line corresponds to the theoretical fits and the points to experimental data. The quartz balance thickness is given in the figure.

growth took tens of minutes, the sampling frequency (7.5–15 spectra per minute) led to nearly real time measurements.

2.2. Spectral evolution, fitting procedure and generic growth scenario

The SDRS spectra shown in figure 1 were recorded during $Ag/Al_2O_3(0001)$ deposition at room temperature. Positive (low energy) and negative (high energy) plasmon absorptions dominated by parallel and perpendicular light-induced dipoles, respectively, characterize a Volmer–Weber growth mode. Percolation of the film grown at 300 K occurs beyond an equivalent thickness of $t = 15$ nm for which the parallel resonance is still above $E = 2$ eV [49] instead of showing a continuous increase of reflectivity at low photon energy, in

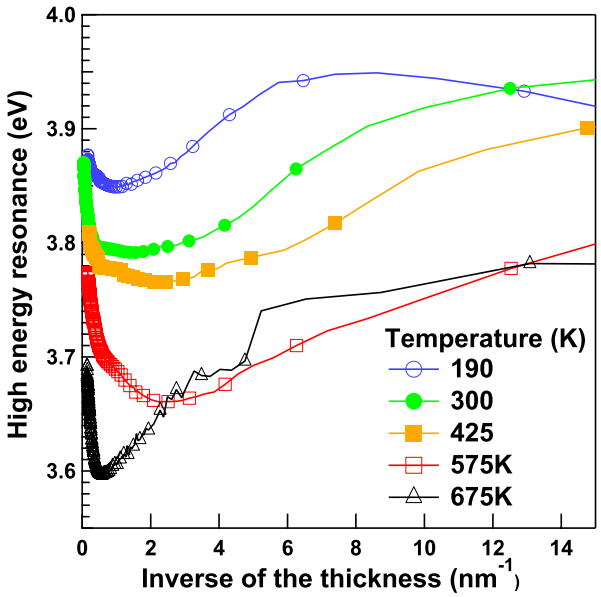

Figure 2. Plot of the high energy resonance position as a function of the inverse of the deposited thickness and of the substrate temperature. The evaporation flux is 0.3 nm s^{-1}.

a similar manner to a continuous film [50]. Upon increasing the silver coverage, the low energy resonance shifts towards lower energy (from 3.25 to 2.5 eV) while the energy position of the high-lying peak is successively red (decrease in size effect) and blue (increase in interparticle interaction) shifted to finally reach a limit of $E = 3.87$ eV close to the perpendicular plasma frequency of a continuous film (figure 2). Indeed, the plasmon resonance of tiny silver particles is blue shifted proportionally to the inverse of the particle size since, as the spill out of the s–p electrons is enhanced by the increasing surface/volume ratio, these electrons undergo less screening by the more localized d-electrons [51]. At the beginning of the growth, this results in a net effect on the high energy peak. As the size increases, the polarizable particle may be viewed in a pure dipole picture as its equivalent dipole corrected from its image [52, 53, 47, 54]. Then, provided that the aspect ratio is constant, the depolarization field created by growing neighbouring particles blue shifts the perpendicular resonance and red shifts the parallel resonance, which qualitatively explains the experimental spectra (figures 1 and 2). The noticeable effect of the temperature that is observed in figure 2 highlights the sensitivity of the plasmonic response to the growth kinetics and film morphology.

The SDRS spectra are fitted (figure 1) by means of the `GRANFILM` program [55] in the framework of the corrected IS model [56]. All technical details about the simulation framework have been given in [49] in which the temperature effects and inhomogeneous broadenings are discussed in the light of a convolution approximation. Constant error bars of $\sigma_{\Delta R/R} = 0.005$ are used in the χ^2-Levenberg Marquardt fitting procedure. The uncertainty in the parameters stems from the χ^2-curvature at the minima. The truncated sphere model [45, 57, 47, 54] used herein to represent clusters corresponds to the equilibrium shape for the isotropic surface

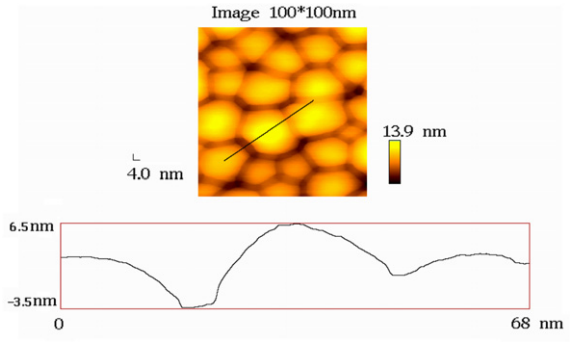

Figure 3. *Ex situ* AFM tapping image of a 5 nm thick silver deposit on $Al_2O_3(0001)$ annealed at $T = 575$ K. The profile shown corresponds to the line drawn on the image.

energy, like for liquid metals. This is reasonable for silver particles that mostly show (100) and (111) facets [58] with almost similar energies [59], although particles annealed at 575 K display hexagonal contours (figure 3) consistent with (111) epitaxy and shape close to a Wulff–Kaischew profile [60, 61]. Finally, at most coverages, in plane anisotropy induced by growth along steps [62, 63] is unlikely because of the low substrate miscut and normal incidence evaporation flux which prevents shadowing effects.

The simulated spectra nicely agree with the data up to an equivalent thickness of $t \simeq 3$ nm. Above that limit, the fit of the low energy resonance worsens (figure 1, lower panel). Upon coalescence, particle reshaping may favour large clusters that escape the truncated sphere model; in addition, the quasi-static approximation is no longer fulfilled as the particle size reaches a sizeable fraction of the optical wavelength ($D \gtrsim 20$ nm). Five free parameters [49] are used to fit the optical data at each temperature: (i) the cluster diameter D, (ii) its aspect ratio $D/H = 2/(1 + t_r)$ (diameter over height) or the particle contact angle θ_c ($\cos(\theta_c) = -t_r$), (iii) the interparticle distance L or the particle density $\rho = 2/\sqrt{3}L^2$ (particles are arranged on an hexagonal lattice in the simulations) and (iv) the two widths of the inhomogeneous broadenings $\sigma_{\parallel,\perp}$ [49]. Simulations were performed at multipolar order $M = 24$ with particle–particle interactions at quadrupolar order and all the interfacial constitutive coefficients $\gamma, \beta, \delta, \tau$ [56, 64]. Figure 4 gives an overview of the evolution of the morphological parameters with temperature at a flux of $F = 0.3$ nm min^{-1}. Size, contact angle (derived from the aspect ratio), density of particles (figure 4) and silver coverage $\Theta = \rho\pi D^2/4$ (figure 5) are determined as a function of the average silver film thickness t. The growth scenario involves two steps, a cluster growth at nearly constant density followed by particle coalescence. The maximum cluster density, the so-called saturation density ρ_s, lies within the range 1–7 $\times$ 10^{12} cm^{-2}. Coalescence reduces this value by a factor of ten. Up to a deposited thickness of ~3 nm, the coverage keeps below the jamming limit of ~55% [65, 9, 66, 5, 67, 68, 1] (the maximum coverage for packing of separated monodisperse discs) (figure 5) and *a fortiori* below the percolation threshold since plasmon resonances are clearly observed [50].

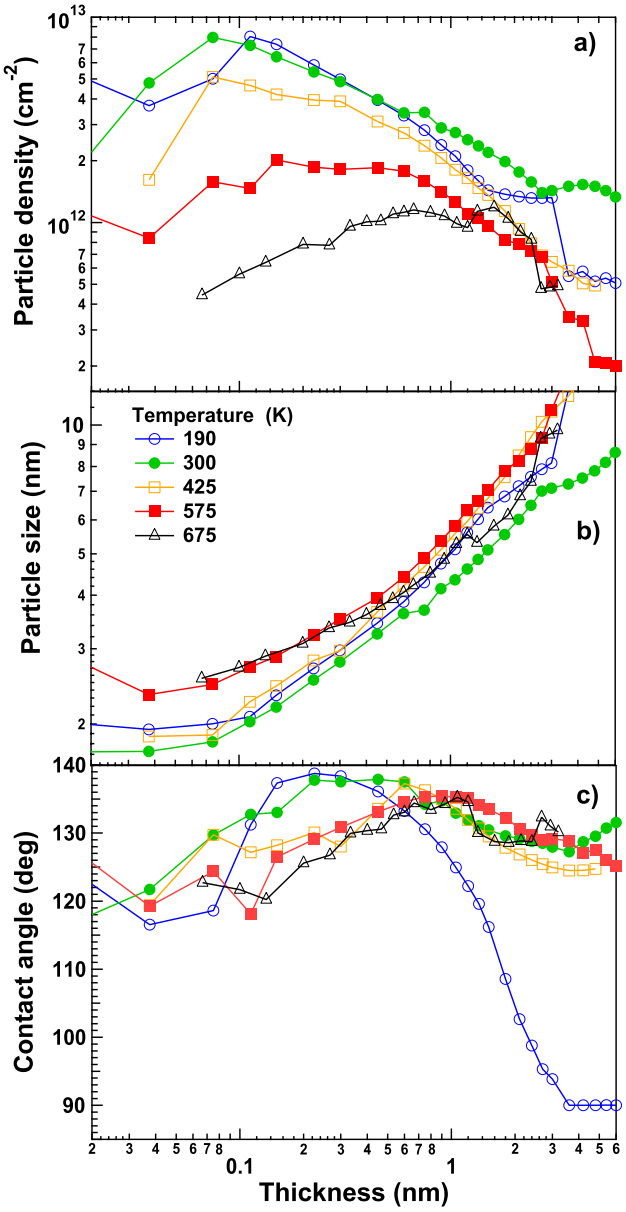

Figure 4. Nanoparticle morphology evolution at various growth temperatures as obtained from the SDRS analysis (flux 0.3 nm min^{-1}). (a) Density ρ. (b) Size D. (c) Contact angle θ_c.

3. Growth mode of Ag nanoparticles on $Al_2O_3(0001)$

Optical measurements achieved *in situ* as a function of substrate temperature and flux allow examination of the physical parameters that combine kinetic and thermodynamic effects. These involve the sticking coefficient, growth laws, saturation density and wetting angles.

3.1. Sticking coefficient and substrate wetting

To first order, the optical SDRS signal varies linearly with the deposited amount (see equations (3.20) of [69]). In figure 6 the thickness t determined by the quartz microbalance is compared to the value $t_{opt} = \rho\pi/8D^3(2/3 + t_r - t_r^3/3)$ (with $t_r = 2H/D - 1$) derived from the fitted parameters

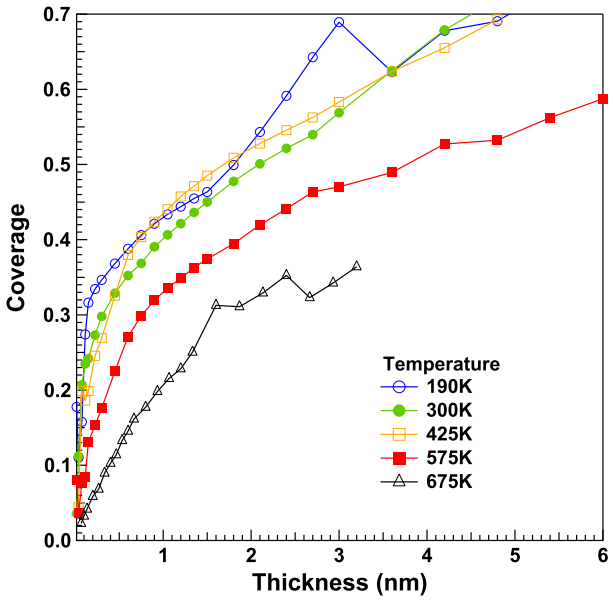

Figure 5. Dependence of the surface coverage $\Theta = \rho\pi D^2/4$ on the temperature during growth (flux 0.3 nm min^{-1}).

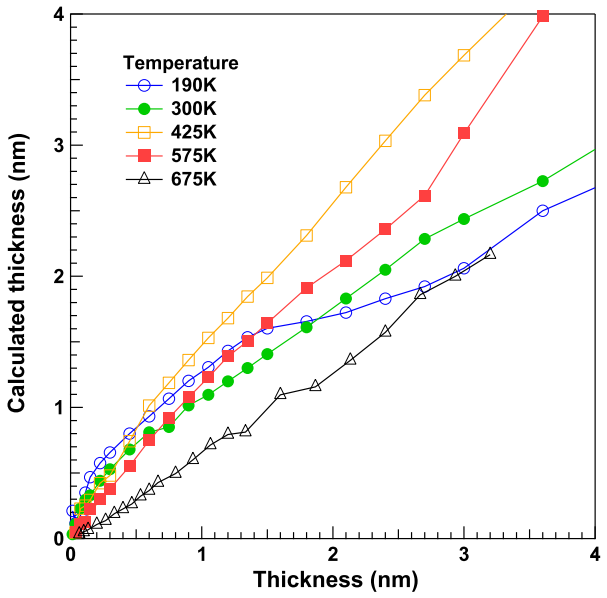

Figure 6. Comparison of the values of the thickness determined by the quartz balance with the values of the thickness t_{opt} derived from the fitted parameters for the various growth temperatures.

assuming that the particles are monodisperse [49]. As already observed for Ag on MgO(001) [37], the striking correlation found between t_{opt} and t leads to an estimate of the sticking coefficient of $S = 1.0 \pm 0.1$ between 190 and 575 K. The decrease to $S = 0.5 \pm 0.15$ at 675 K is assigned to incomplete condensation. A similar trend was reported by Van Campen and Hrbek [70] who found sticking coefficients of 0.8–0.9 up to 400 K and zero at 500–600 K on both α-$Al_2O_3(11\bar{2}0)$ and alumina films on Ru. The discrepancy may lie in the accuracy of temperature measurement and in the effect of the deposition rate. Indeed, in measurements at 575 K, S drops from unity at a flux of 0.3 nm min^{-1} to 0.7 ± 0.15 when the flux is decreased by a factor 4.

The substrate coverage is given independently of the particle shape by $\Theta = \rho\pi D^2/4$. As shown in figure 5, the higher the temperature is the lower the coverage is for the same amount of matter, as expected for thermally induced dewetting and reduced sticking coefficient. Θ sharply increases up to 30–40% for $t < 0.5$ nm at low temperatures ($T \leq 425$ K). For temperatures higher than $T = 575$ K, the coverage stays below the percolation threshold [65, 66, 5, 67, 68] of ∼70% for random growth of 3D particles. Conversely, at 190 K, the reduced atomic mobility results in a steep increase of the coverage above $t \simeq 3$ nm. This correlates with the observed flattening of the particles (see below and figure 4(c), $T = 190$ K) and with poorer fits (see figure 1, lower panel). At this stage [66], coalescence makes the truncated sphere shape model questionable and the quasi-static approximation starts breaking down as the particle diameter becomes non-negligible with respect to the optical wavelength ($D \gtrsim 20$ nm). This scenario is qualitatively confirmed by annealing a film grown at 190 K (figure 7). Up to 625 K, the blue shift of the low energy resonance is indicative of both reduction in particle density and increase in aspect ratio; the thickness remains nearly constant as evidenced by the integrated SDRS signal (not shown) (figure 7(a)). From 625 to 900 K, the decrease in optical intensity at constant energy shows that silver desorbs while the particles keep a constant aspect ratio (figure 7(b)). Consistently, particles deposited at high temperature (675 K) that are close to equilibrium shape only shrink through metal desorption upon annealing (figure 7(c)).

3.2. Nucleation on defects and evolution of the saturation density with temperature

The saturation density ρ_s is defined as the maximum particle density that is reached at the end of the nucleation regime. Saturation is observed for both nucleation on defects and homogeneous nucleation [71] because the consumption of monomers by the already nucleated clusters hinders the aggregation of sub-critical entities. For $Ag/Al_3O_3(0001)$, at a given temperature, the cluster density is nearly constant up to the coalescence threshold t_t (figure 4). Figure 8 displays the average value ρ_s in an Arrhenius graph as a function of $1/T$. The constant density at $T \leq 300$ K followed by a density decrease at $T \geq 425$ K clearly favours a nucleation on defects instead of a homogeneous nucleation. Similar observations were made for Fe and Co particles on $CaF_2(111)$ [72], and Pd [40] and Ag [73] clusters on MgO(001). By introducing a Langmuir-like isotherm to treat the temperature dependence of the defect occupancy, Venables [74, 71, 72, 40, 75] explained theoretically such a behaviour by extending the theories of rate equations [76, 71, 74, 77] to treat growth at defect sites. This idea was somehow previously introduced by Markov and Kashchiev [78, 79] through supersaturation-dependent defect activity. All defects are decorated by clusters until, at a high enough temperature ($T \geq 425$ K, figure 8), thermal fluctuations overcome the trap well energy. Detrapping occurs at a much lower temperature

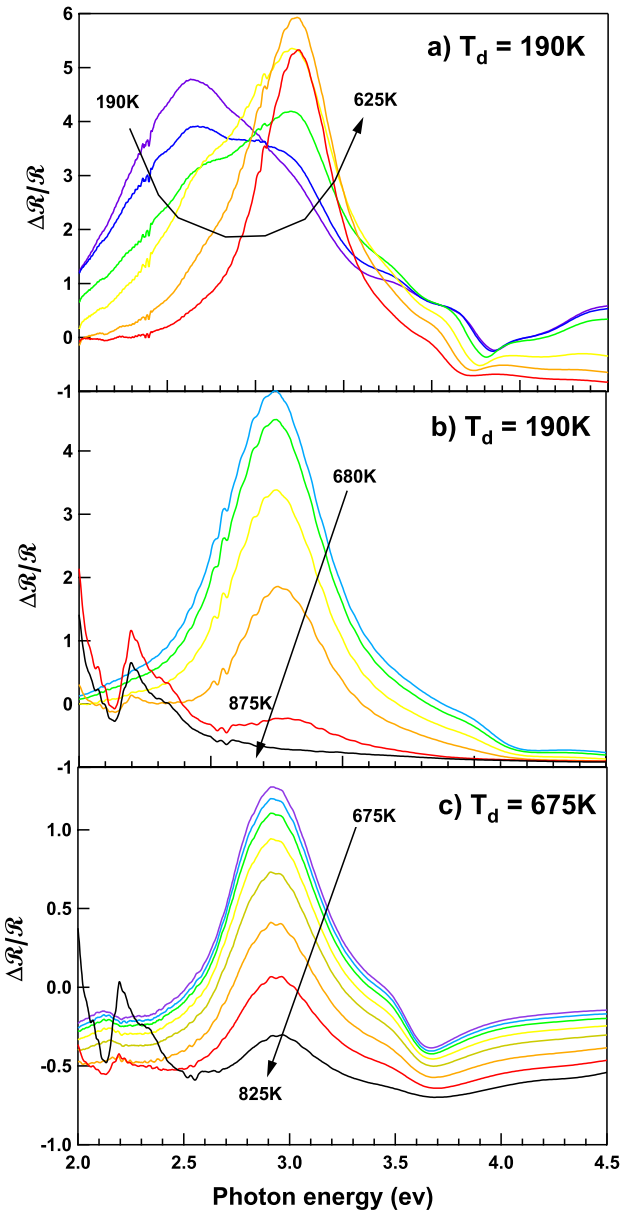

Figure 7. SDRS signal during $Ag/Al_2O_3(0001)$ sample annealing. (a), (b) 6 nm deposited at $T_d = 190$ K. (c) 7.5 nm deposited at $T_d = 675$ K. The 6 nm thick film deposited at 675 K is annealed from 190 to 625 K in (a), and then up to 875 K in (b), a temperature at which the desorption of silver is almost completed. An evolution comparable to that seen in (b) is observed in (c) upon annealing a film deposited at 675 K up to 825 K. The spectra were not corrected for substrate thermoreflectance.

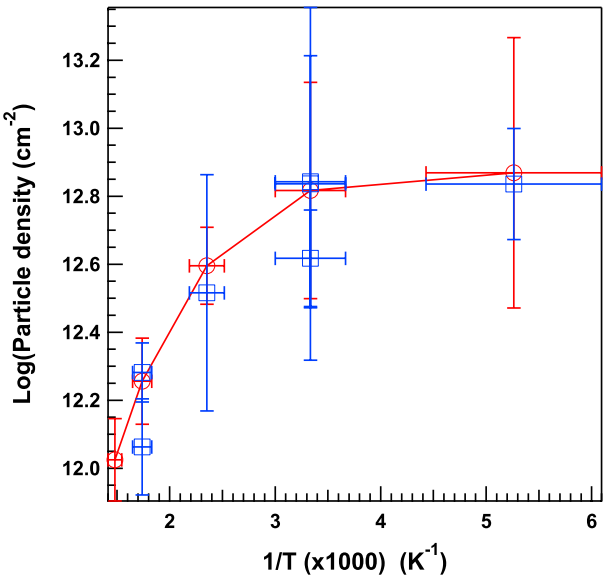

Figure 8. Logarithm of the saturation density ρ_s (particle cm^{-2}) versus the inverse of the growth temperature. Circles: flux of 0.3 nm min^{-1}; squares: flux of 0.075 nm min^{-1}.

for Ag/alumina than for Pd/MgO [40], a fact explained by a weaker interaction with wide band gap oxide. It was not observed for Ag/MgO(001) [73] for $T \geq 300$ K. The high temperature Arrhenius dependence of ρ_s gives a slope of 710 ± 170 K corresponding to an activation energy of $E_{act} = 0.06 \pm 0.015$ eV, in close agreement with experimental measurements on Ag/MgO(001) [73] and Au/MgO(001) [80]. This value cannot be assigned in a straightforward way [80] either to adsorption or to diffusion energy of adatoms [74, 71], as the nucleation observed herein is clearly not homogeneous. Indeed random nucleation in the regime of incomplete condensation [77, 71] for stable clusters made of two atoms ($i = 1$) gives $E_{act} = (4E_a - E_d)/3$ where E_a and E_d are the adsorption and diffusion energies of single atoms. Therefore, the density functional theory value of $E_a \simeq 0.5$ eV [81] would lead to an $E_d < 0$ unphysical value. At the other extreme limit of complete condensation (a reasonable hypothesis here except at $T = 675$ K), homogeneous nucleation gives $E_d = \frac{7}{2}E_{act} = 0.21$ eV. This value, which corresponds to the expected order of magnitude for the diffusion of noble metal on bulk insulating substrate [71, 75], is close to the calculated activation barrier for diffusion on an Al-terminated surface $E_d = 0.25$ eV [81]. Nevertheless, it should be taken with caution as the role of defects cannot be ignored.

For most measurements, the acquisition time of SDRS spectra hardly allows for the grasping of the nucleation stage during which ρ increases (although some premises are seen in figure 4). However, nucleation is observed at small flux (0.075 nm min^{-1}) and high temperature (575 K), as depicted in figure 9. A break in slope for the size growth ($D \sim t^{0.1\pm0.3}$ to $D \sim t^{0.33\pm0.1}$) separates nucleation at nearly constant size from growth at nearly constant density. Interestingly, the particles during nucleation are the most adhesive ones (see figure 10 and section 3.4). With the flux under study, the minimum time to saturate all the defects by single atoms is of the order of $\tau_s \simeq \rho_s/F \simeq 1$ s, corresponding to an equivalent thickness of $t_s \simeq 10^{-3}$ nm. Fortunately, it may be modified by desorption of adatoms, imperfect trapping on defects and competition between nucleation and growth upon increasing temperature [71]. Robins and Rhodin [82] modelled the nucleation on defects by assuming that nucleation only occurs on defects acting as perfect traps and that only adatoms are mobile. In a regime of incomplete condensation where the diffusion length of adatoms is smaller than the distance between traps, an exponential time dependence for the cluster

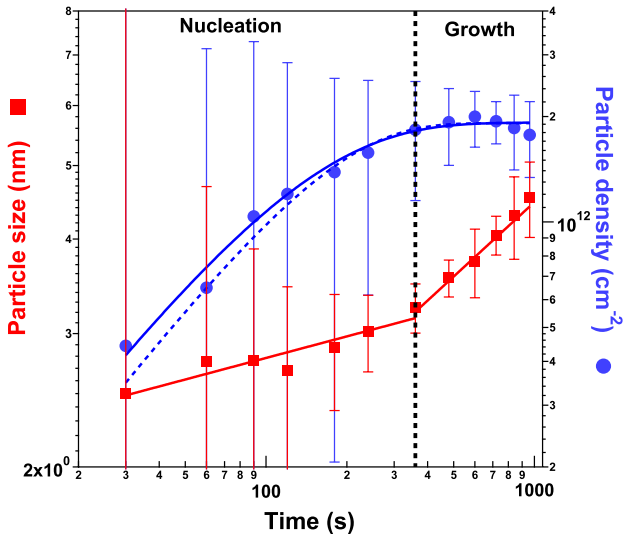

Figure 9. Evolution of the size and density for the growth at $T = 575$ K and a flux of 0.075 nm min^{-1} showing particle nucleation followed by growth. Fits with equation (1) of Robins and Rhodin [82] (solid line) and equation (2) of Markov and Kaschchiev [78, 85] (dotted line) for the density or power law fits of the size from $D \sim t^{0.1\pm0.3}$ to $D \sim t^{0.33\pm0.1}$ are shown in the figure.

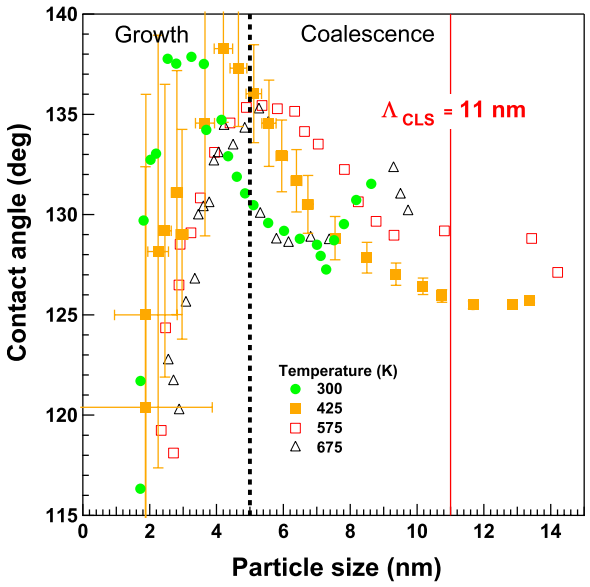

Figure 10. Evolution of the contact angle θ_c for several temperatures as a function of the particle size. Note that the growth and coalescence regimes (see figure 11 for example) are related to the main evolutions of the wetting angle (see text). The line sets the expected onset of the first dislocation appearance $D = \Lambda_{CLS}/\sin(\theta_c)$ corresponding to the distance $\Lambda_{CLS} = 11$ nm at the interface. Typical error bars are given for the 425 K growth.

density is found:

$$\rho = \rho_0^{RR}[1 - \exp(-J_0^{RR}\tau)]. \quad (1)$$

Here J_0^{RR} is the nucleation rate, ρ_0^{RR} is the saturation density assigned to the trap density and τ is the time. Similar results are found in [83, 84]. Markov and Kaschchiev [78, 85] improved the model by accounting for zones around the growing nuclei where nucleation is forbidden. Assuming a diffusive growth $L_d = c\sqrt{\tau}$ of this zone under the same hypotheses as Robins and Rhodin, they found

$$\rho = \rho_s^{MK}\left[1 - \frac{\mathrm{erfc}(A/2 + J_0^{MK}\tau/A)}{\mathrm{erfc}(A/2)}\right] \quad (2)$$

where erfc is the error function. The saturation density ρ_s^{MK} and A are given by

$$A = \sqrt{\frac{6J_0^{MK}}{\pi c^2 \rho_0^{MK}}};$$
$$\rho_s^{MK} = \rho_0^{MK}\frac{\sqrt{\pi}}{2}A\exp(A^2/2)\mathrm{erfc}(A/2) \quad (3)$$

as functions of the nucleation rate J_0^{MK} and the density of defects ρ_0^{MK}. Markov and Kaschchiev showed that their model reverts to the model of Robins and Rhodin when the growth rate of the influence zone c is zero. Of course, the situation becomes incredibly more complex if a distribution of active centre potentials c is accounted for [79]. Both models agree with the data of figure 9 with similar trap densities ($\rho_0^{RR} = 1.9 \times 10^{12} \pm 1.8 \times 10^{11}$ cm^{-2}; $\rho_0^{MK} = 1.7 \times 10^{12}$ cm^{-2}), although they differ by a factor of 2 on the nucleation rate ($J_0^{RR}\rho_0^{RR} = 1.5 \times 10^{11}$ cm^{-2} s^{-1}; $J_0^{MK}\rho_0^{MK} = 7.2 \times 10^{10}$ cm^{-2} s^{-1}). The fitted speed of

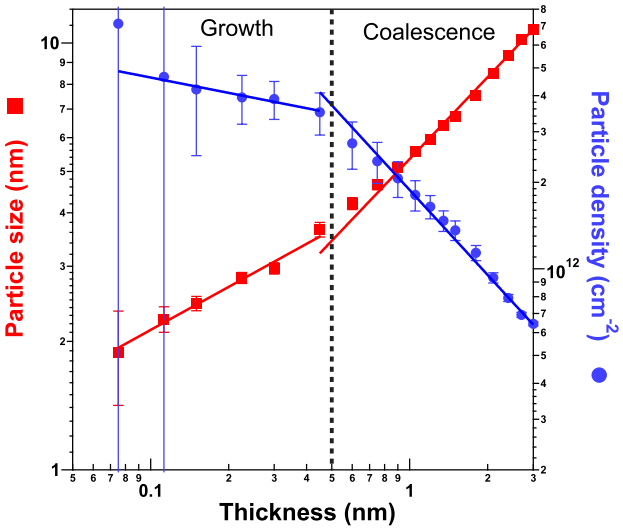

Figure 11. Power law fits of the size and density evolution ($T = 425$ K, flux 0.3 nm min^{-1}), highlighting the separation at thickness t_t from growth ($\rho \sim t^{-0.1\pm0.3}$ and $D \sim t^{0.3\pm0.1}$) and coalescence ($\rho \sim t^{-0.9\pm0.3}$ and $D \sim t^{0.6\pm0.03}$).

screening zone growth $c = 0.5$ nm s$^{-1/2}$ is compatible with a diffusion coefficient [78] of $D = c^2 \simeq 2.3 \times 10^{-15}$ cm^2 s^{-1}. The agreement of the present data with models relative to heterogeneous nucleation suggests that not all defects are populated at this temperature (see figure 8).

3.3. Growth and coalescence mechanisms: the exponents

Log–log plots of the particle size and density reveal power laws with a break in slope as illustrated in figure 11 at

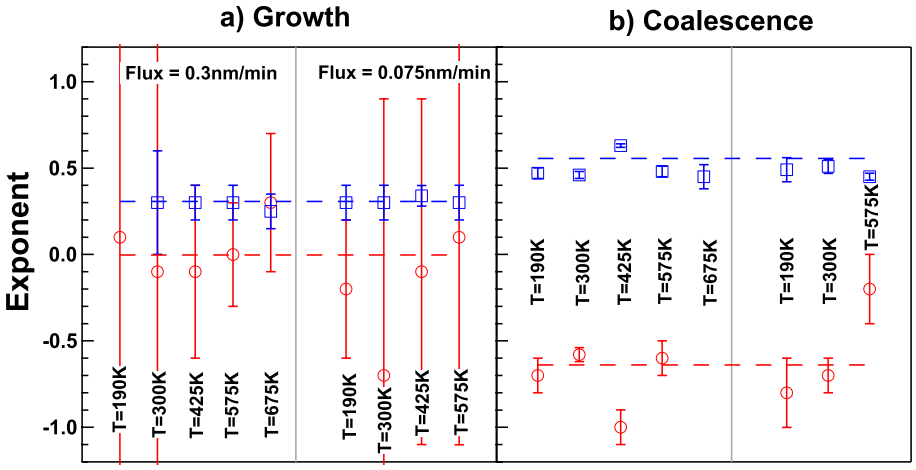

Figure 12. Power law exponents for all the deposit conditions of density (circles) and size (squares). The dotted lines give the average values of (a) $D \sim t^{0.31\pm0.03}$, $\rho \sim t^{0\pm0.2}$ during growth and (b) $D \sim t^{0.55\pm0.01}$, $\rho \sim t^{-0.64\pm0.03}$ during coalescence.

425 K or in [49] at 575 K. The analysis of the slopes was performed at all temperatures and fluxes below the limit of $\Theta = 55\%$ and, of course, below the percolation threshold. In the static picture of coalescence [8, 9, 1], this universal value of coverage corresponds to a balance between coalescence and particle spreading due to growth. The synopsis of fitted exponents reveals a general trend (figure 12). Up to the temperature-dependent threshold t_t, the cluster density is nearly constant ($\rho \sim t^{0\pm0.2}$ on average). The cluster size dependence ($D \sim t^{0.31\pm0.03}$) is consistent with a growth mechanism limited by adatom diffusion in the cluster capture area ($D \sim t^{1/3}$) instead of peripheral attachment [86, 11]. Underlying assumptions of full condensation with a negligible direct impingement on the particle seem to be fulfilled since the sticking coefficient is close to one (figure 6) and the coverage is still low. Analytical solutions of the diffusion equation around an isolated particle growing from a constant flux at infinity [32], or from a concentration of adatoms on a regular lattice of particles [87], or a fluid-dynamic model of droplet condensation [16] lead to the same $D \sim t^{1/3}$ power law which pictures particles growing on their capture area without merging with neighbouring objects and without further nucleation. A similar exponent is found for breath figures or dew formation at a scale of 1 μm/1 mm [7, 8, 1]. This was discussed on the basis of simple scaling arguments [11] by Beysens *et al* [6] in a parallel drawn between macroscopic liquid droplets and deposited metal clusters (namely Ag on amorphous carbon). Values close to 0.3 were also found for metal/oxide growths studied by x-ray scattering (Au/TiO_2(110) [36], Pt/MgO(001) [35], Ag/MgO(001) [38]) and *ex situ* microscopy techniques (see [4, 87] and references therein). This $D \sim t^{0.31}$ behaviour gives also a hint about the nucleation process by discarding homogeneous nucleation for which a 1/2 exponent is expected from fluid dynamics analysis [16], while a 1/3 exponent is found for heterogeneous nucleation. From the literature results of the rate equations of solid/solid growth [74, 84], nucleation on defects ($D \sim t^{1/3}$) is more likely than homogeneous nucleation for which a $D \sim t^{2/9}$ law is predicted. This conclusion is in line with the section 3.2 about the temperature dependence of the saturation density.

Coalescence occurs above the threshold t_t which is a turning point for the growth process. Beyond t_t, the particle density decreases ($\rho \sim t^{-0.64\pm0.03}$), the size grows at a higher rate ($D \sim t^{0.55\pm0.01}$) (figure 11) and the increase in coverage slows down (figure 5). The present findings strongly differ from the $D \sim t$ scaling relative to static coalescence [11–14, 9, 15, 16, 25, 88]. Moreover, Vincent's equation [89, 14, 67] of coalescence $\rho \sim -\Theta$ which linearly links density and coverage is not fulfilled since, on average, $\Theta \sim t^{0.29\pm0.05}$. Regarding the particle density, the discrepancy is even stronger; Family and Meakin's simulations of static coalescence [12, 13, 9] predict an exponent of -0.27 for homogeneous nucleation, upon adding new droplets, and close to -0.37 for heterogeneous nucleation, when droplets are nucleated randomly and grow at a rate proportional to the particle size. The good agreement of the power laws found herein ($D \sim t^{0.55\pm0.01}$ and $\rho \sim t^{-0.64\pm0.03}$) with those of Steyer *et al* [32] ($D \sim t^{0.48}$ and $\rho \sim t^{-0.45}$) favours the dynamic mechanism, despite a discrepancy in the coverage scaling ($\Theta \sim t^{0.56}$ instead of $\Theta \sim t^{0.29\pm0.05}$ herein) and range (below 0.2 in the simulations and above in this work). Large clusters which are predicted to drive the coalescence mechanism described by Steyer *et al* [32] are expected to dominate the optical response, the intensity of which is proportional to the volume of matter $V \sim D^3$. Finally, the values of the coverage corresponding to the onset of coalescence (figure 13) depend on the temperature and flux. A constant value close to 30% [8, 9, 1] would be expected for static coalescence. An amazing parallel can be drawn with experiments and simulations [26] on water condensation on solid benzene near its melting point. The release of condensation heat above a critical size locally melts the substrate, relaxes strains at the contact line and triggers a jump of the particle [90] that enhances coalescence with an intermediate $D \sim t^{0.5}$ behaviour before reaching linear behaviour [26]. The discrepancy with the exponent expected for static coalescence might also partly arise from direct

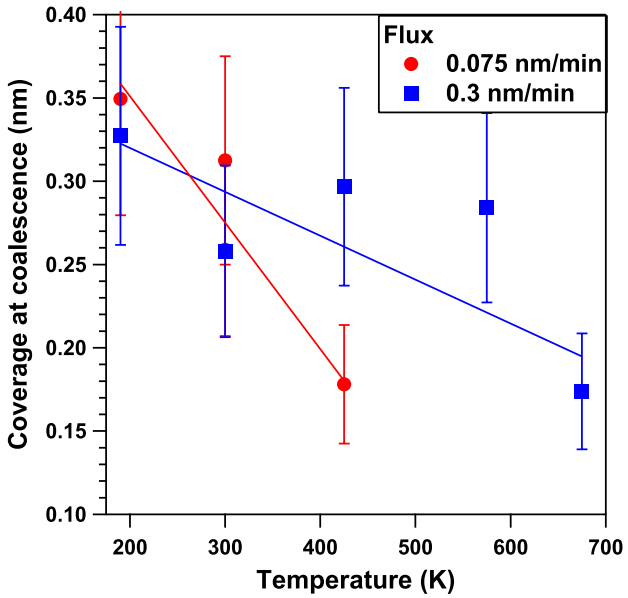

Figure 13. Surface coverage at the transition between the growth regime and the coalescence regime as a function of the substrate temperature and the evaporation rate. The regression lines are guides for the eyes.

impingement of silver from the vapour on the clusters [32]. Such a process increases with coverage, with an expected $D \sim t^{2/3}$ power law (the trapped amount is proportional to the area of the cluster [10]). However, since the coverage is below 0.3 at the onset of coalescence, this phenomenon cannot dominate the growth rate of the particles which is therefore consistent with an involvement of particle diffusion.

The diffusion of particles [91] may happen either through peripheral evaporation/condensation of atoms [92–94], or dislocation movement, or concerted translation–rotation [95, 96], or diffusion of particles as a whole [29, 97, 30, 31]. The diffusion of adatoms implied by the first two mechanisms dominates strong epitaxy (in particular metal on metal [98]). The latter two mechanisms are favoured by either poor matching or weak bonding. Dedicated experiments [18, 19] have demonstrated the size-dependent diffusion of Au particles of 2–3 nm in size on alkali-halide and assigned it to a sliding of the interface [20, 21] up to a locking in an epitaxial energy minimum. When the interface is not commensurate, earlier modelling of rotation and translation of islands [27, 28] and more recent molecular dynamics simulations [29–31] have shown that the modulation of the potential felt by the centre of mass of the particle is small enough to allow diffusion in a Brownian motion or even a stick/slip motion through Levy flight excited by thermal vibrations. In this case, the gains and losses of potential energy of the interface atoms are balanced upon translation. For particles nucleated on defects, the contribution of the trap well to the interface energy is expected to become negligible upon growing [19, 25, 31]. Even on amorphous substrates, vapour grown [25] or deposited [22–24] clusters involving thousands of atoms are suggested to move. Such counter-intuitive mechanisms may result in diffusion coefficients similar to or even higher than those of single adatoms [27, 18, 28, 22, 91] and clusters with hundreds of atoms may diffuse as well as single atoms [30]. Notably, the onset of coalescence t_t (figures 4 and 10) corresponds herein to the maximum of the contact angle (lowest adhesion energy). In line with previous results [36, 38] and in agreement with earlier expectations about reusable nucleation sites [99], diffusion may be enhanced above a critical size [25] while the smallest particles remain trapped on defects. The introduction of interface dislocation leading to an incoherent interface may trigger the phenomenon as was suggested for magic 2D island sizes [95].

3.4. Change in wetting through growth and coalescence regimes

The sizes (figure 4(b)) and contact angles (figure 4(c)) evolve in parallel, except for high coverages at 190 K as the kinetics comes into play; at 190 K, the steep increase in coverage from $t \simeq 3$ nm (figure 5) reveals an early coalescence that correlates with a drop in contact angle (figure 4(b); $T =$ 190 K). An extra proof of these kinetic effects is given by the decrease with temperature of the inhomogeneous contribution $\sigma_{\parallel}$ to the broadening of the plasmon peaks which scales with the aspect ratio distribution (see [49]). A common picture of the size dependence of the contact angle θ_c emerges between 425 and 675 K, a temperature range selected to rule out kinetic effects [49]. In figure 10, θ_c is plotted as a function of the particle size obtained from analysis. It appears lower than 120° for small clusters ($D \simeq 2.5$ nm) and increases up to 135°–140°for particle sizes corresponding to the very end of the growth ($D =$ 4 nm) (figure 11). It then levels off ($D \simeq 4$–6 nm) at the beginning of the coalescence and finally, for size $D \geq 9$ nm, drops to a final value which on average amounts to $\theta_c =$ 127.5° ± 1°, in agreement with macroscopic sessile drop measurements on melted metal in a regime of low oxygen activity ($\theta_c = 128° \pm 4°$, [100], and $\theta_c = 110°$–130°, [101]), *ex situ* transmission electron microscopy measurements ($\theta_c =$ 125°, [102]) and previous data ($\theta_c = 127° \pm 4°$, [48]). Taking $\sigma_{Ag} = 1.24$ J m^{-2} for the silver surface energy [103], the Young–Dupré equation gives an adhesion energy of $E_{adh} = \sigma_{Ag}[1 + \cos(\theta_c)] = 0.48 \pm 0.02$ J m^{-2}. Similar values have been obtained for silver multilayers on alumina by density functional theory ($E_{adh} = 0.33/0.38$ J m^{-2}, [44, 101]), full potential linearized augmented plane waves ($E_{adh} = 0.549$ J m^{-2}, [41, 42] in the generalized gradient approximation) and for a silver monolayer by Hartree–Fock simulations ($E_{adh} = 0.17$–0.27 J m^{-2}, [43]). All modellings agree with a physisorption of silver with negligible charge transfer and weak atomic polarization.

The changes in contact angle that are seen in figure 10 for particles less than 10 nm in size run counter to the Wulff–Kaishew size-independent equilibrium shape [60]. The many origins of this size dependence [104] involve the elastic strain due to the lattice mismatch with the substrate [104–108], the surface stress or Laplace overpressure [109, 104, 110], the variations of the interface/surface energies and, therefore, of the adhesion energy [111–113] and the interface line energy [104, 114] as discussed

by thermodynamic approaches [106–108, 104, 114] and atomistic simulations [111, 112, 105].

For an expected $[11\bar{2}](111)_{Ag} \parallel [10\bar{1}0](0001)_{Al_2O_3}$ epitaxial relationship, the interface lattice parameters of $Ag/Al_2O_3(0001)$ ($a_{Ag}^{[11\bar{2}]} = 0.5003$ nm; $a_{Al_2O_3}^{[10\bar{1}0]} = 0.4785$ nm) lead to $m = \frac{a_{Ag}-a_{Al_2O_3}}{a_{Al_2O_3}} = 4.6\%$. It is worth comparing Ag/alumina to Ag/MgO(100) (cube on cube $[100](001)_{Ag} \parallel [100](001)_{MgO}$ epitaxy) for which the mismatch $m = \frac{a_{Ag}-a_{MgO}}{a_{MgO}} = -2.9\%$ ($a_{Ag}^{[100]} = 0.4090$ nm; $a_{MgO}^{[100]} = 0.4212$ nm) is negative. For growing Ag/MgO(100), the silver lattice parameter is smaller than that of bulk silver for clusters smaller than 2 nm in size (0.395 ± 0.07 nm). It then increases under the influence of mismatch-induced strain as the clusters grow (∼3–4 nm) until it nearly fits the MgO parameter [110]. It finally decreases to reach the bulk parameter of silver [110]. The initial contraction of the silver lattice in Ag/MgO(100), that cannot stem from mismatch, can be instead assigned to surface stress that is active because the adhesion energy is weak ($E_{adh} = 0.8$ J m^{-2}, [37, 38]). The parameter contraction of $3.5 \pm 1.8\%$ determined for Ag clusters of 1.5 ± 0.4 nm in size [110] is in rather good agreement with the contraction of 1–2% calculated for silver clusters of similar size [115]. Surface stress is therefore expected to decrease the parameters of silver clusters smaller than ∼5 nm in size [115]. In the case of Ag/alumina, such a contraction of the parameter should result in a decrease of the lattice mismatch and, consequently, in an improvement of the adhesion energy and in a decrease of the wetting angle [111, 112, 116–118]. Moreover, below $D = 4$ nm, elastic strain likely participates in a contraction of the silver lattice (although anharmonic interatomic potentials result in different profiles for tensile (Ag/MgO) or compressive (Ag/alumina) islands [105]). Therefore, for $D \leq 4$ nm, in the growth regime (figure 11), the increase in contact angle θ_c that accompanies the increase in size of the particles (figure 10) likely relies on the elastic response of the particles.

From $D \simeq 4$–6 nm to $D \simeq 20$ nm (figure 10), as the particles coalesce, the Ag/alumina particles show a progressive decrease in contact angle. Using linear elasticity, Müller and Kern [106–108] included the mismatch-induced strain in the Wulf–Kaishew [60] theorem. They showed that epitaxial strain acts against wetting whatever the sign of the misfit and that the appearance of each interface dislocation relaxes the stored elastic energy to abruptly alter the equilibrium shape. Similar conclusions were drawn by the finite-element approach of Wong and Thouless [119] for the truncated sphere shape and by atomistic simulations [111, 112]. Therefore, the decrease in contact angle observed above $D \simeq 6$ nm is attributed to plastic deformation. Upon further increase in particle size, a coincidence lattice site (CLS) develops with a period of $\Lambda_{CLS} = a_{Al_2O_3}^{[10\bar{1}0]} a_{Ag}^{[11\bar{2}]} / (a_{Al_2O_3}^{[10\bar{1}0]} - a_{Ag}^{[11\bar{2}]}) = 11$ nm. Assuming a perfect match at the core of the island, the Vernier rule predicts the introduction of the first dislocation at a particle interface size $D_i = D\sqrt{1 - t_r^2} = D\sin(\theta_c)$ given by the separation between areas of good and poor match at the interface, leading to $D = \Lambda_{CLS}/\sin(\theta_c) \simeq$ 14 nm. The expectation that such a value corresponds to the asymptotic value of the contact angle [107, 108] is consistent with the observation (figure 10). Finally, as shown in the appendix, an elastic deformation of the interface up to a value given by the bulk lattice mismatch would give rise to a contact angle variation of $\Delta\theta_c = +2.5°$, the order of magnitude of which agrees with the observed one. This reinforces an explanation of contact angle variation based on the strain effect.

4. Conclusions and outlook

Surface differential reflectivity spectroscopy (SDRS) in the UV–visible range was used to analyse *in situ* the nucleation, growth and coalescence of Ag nanoparticles on $Al_2O_3(0001)$. Supported clusters were represented by truncated spheres. The modelling of data that was based on the determination of surface susceptibilities was quite successful in determining the size, shape (aspect ratio and contact angle) and density of the silver particles. The main characteristics of the growth process are as follows.

(i) Nucleation and growth on defects are evidenced up to 300 K.

(ii) The power laws $D \sim t^{0.31}$ and $D \sim t^{0.55}$ were found in the growth and coalescence regimes, respectively. These are representative of the system since these parameters were reproducible over the whole temperature range at different fluxes. The $D \sim t^{0.31}$ law is attributed to the growth of isolated particles from their influence area at fixed position. Most importantly, the $D \sim t^{0.55}$ law which is not consistent with static coalescence favours instead dynamic coalescence. The kinetic character of the coalescence, the onset of which occurs at a coverage which decreases when either the temperature increases of the flux decreases, supports such an assumption.

(iii) The wetting angle of the Ag/alumina particles is seen to increase from $\theta_c = 119°$ to 137° during the growth stage. Conversely, it slowly decreases towards $\theta_c = 127°$ during the coalescence. These behaviours are attributed to elastic and plastic strains, respectively.

These results highlight (i) the dramatic changes that occur in the wetting of supported nanoparticles during their growth and coalescence and (ii) the involvement of the kinetics in the growth/coalescence mechanism. The plasmonic technique is revealed to be a unique *in situ* technique to pinpoint such rarely observed effects by allowing an accurate determination of the morphologies and wetting angles of particles of approximately a nanometre in size. Beyond the case of growth on surfaces, this work opens strong perspectives in important fields involving supported metallic nanoparticles such as heterogeneous catalytic reactions [120], catalysed chemical vapour growth of carbon nanotubes or even gas sensing [121].

Acknowledgment

We would like to acknowledge Pascal Naël from Saint-Gobain Recherche for his technical assistance.

Appendix. Variation of the contact angle upon interface strain

The goal of this appendix is to obtain an estimate of the variation of the contact angle upon an isotropic stain of the interface assuming that the truncated sphere shape is kept. The volume of the truncated sphere is given by a straightforward integration:

$$V = \pi/8D^3[\tfrac{2}{3} - \cos(\theta_c) + \tfrac{1}{3}\cos(\theta_c)^3] \qquad (A.1)$$

while the interface size reads $D_i = D\sin(\theta_c)$. Therefore, $V = \pi/8D_i^3F(\theta_c)$ with

$$F(\theta_c) = \frac{1}{\sin^3(\theta_c)}\left[\frac{2}{3} - \cos(\theta_c) + \frac{1}{3}\cos^3(\theta_c)\right]. \qquad (A.2)$$

Assuming that the deformation is performed at constant volume, one obtains

$$\begin{aligned} \Delta\theta_c &= -3\frac{\Delta D_i}{D_i}\frac{F(\theta_c)}{(\partial F/\partial\theta_c)\,(\theta_c)}; \\ \left(\frac{\partial F}{\partial\theta_c}\right)(\theta_c) &= 1 - 3\cot(\theta_c)F(\theta_c). \end{aligned} \qquad (A.3)$$

The equilibrium contact angle $\theta_c = 130°$ and the lattice mismatch between alumina and silver $\Delta D_i/D_i = (a_{Ag} - a_{Al_2O_3})/a_{Ag} = -4.3\%$ yield $\Delta\theta_c = 2.5°$. If the Poisson ratio of silver ($\nu = 0.37$) is taken into account (even though the geometry is not exactly the right one!), the relative variation of the volume should read $\frac{\Delta V}{V} \simeq (1-2\nu)\frac{\Delta D_i}{D_i}$. Therefore, the coefficient 3 in equation (A.3) should be replaced by a factor $2(1+\nu) = 2.74$ which does not change the order of magnitude drastically.

References

[1] Beysens D 2006 Dew nucleation and growth *C.R. Phys.* **7** 1082–100

[2] Zinke-Allmang M, Feldman L C and Grabow M H 1992 Clustering on surfaces *Surf. Sci. Rep.* **16** 377–463

[3] Campbell C T 1997 Ultrathin metal films and particles on oxide surfaces: structural, electronic and chemisorptive properties *Surf. Sci. Rep.* **27** 1–111

[4] Henry C 1998 Surface studies of supported model catalysts *Surf. Sci. Rep.* **31** 231–325

[5] Zinke-Allmang M 1999 Phase separation on solid surfaces: nucleation, coarsening and coalescence kinetics *Thin Solid Films* **346** 1–68

[6] Beysens D, Knobler C M and Schaffar H 1990 Scaling in the growth of aggregates on a surface *Phys. Rev.* B **41** 9814–8

[7] Beysens D and Knobler C M 1986 Growth of breath figures *Phys. Rev. Lett.* **57** 1433–6

[8] Fritter D, Knobler C M and Beysens D 1991 Experiments and simulation of the growth of droplets on a surface (breath figures) *Phys. Rev.* A **43** 2858–69

[9] Meakin P 1992 Droplet deposition, growth and coalescence *Rep. Prog. Phys.* **55** 157–240

[10] Leach R N, Stevens F, Langford S C and Dickinson J T 2006 Dropwise condensation: experiments and simulations of nucleation and growth of water drops in a cooling system *Langmuir* **22** 8864–72

[11] Viovy J L, Beysens D and Knobler C M 1988 Scaling description for the growth of condensation patterns on surfaces *Phys. Rev.* A **37** 4965–70

[12] Family F and Meakin P 1988 Scaling of droplet-size distribution in vapor deposited thin films *Phys. Rev. Lett.* **61** 428–31

[13] Family F and Meakin P 1989 Kinetics of droplet growth processes: simulations, theory and experiments *Phys. Rev.* A **40** 3836–54

[14] Briscoe B J and Galvin K P 1991 Growth with coalescence during condensation *Phys. Rev.* A **43** 1906–17

[15] Zinke-Allmang M, Feldman L C and Van Saarloos W 1992 Experimental study of self-similarity in the coalescence growth regime *Phys. Rev. Lett.* **68** 2358–61

[16] Kuz V A 1994 Dynamics of the condensation of a saturated vapor into droplets *Phys. Rev.* E **49** 1246–50

[17] Renaud G *et al* 2003 Real time *in situ* quantitative study of growing islands by grazing incidence small-angle x-ray scattering *Science* **300** 1416–9

[18] Masson A, Métois J J and Kern R 1971 Migration brownienne de cristallites sur une surface et relation avec l'épitaxie. I Partie expérimentale *Surf. Sci.* **27** 463–82

[19] Métois J J 1973 Migration brownienne de cristallites sur une surface et relation avec l'épitaxie. IV. Mobilité de cristallites sur une surface: décoration de gradins monoatomiques de surface *Surf. Sci.* **36** 269–80

[20] Kern R, Masson A and Métois J J 1971 Migration brownienne de cristallites sur une surface et relation avec l'épitaxie. II. Partie théorique *Surf. Sci.* **27** 483–98

[21] Métois J J, Gauch M, Masson A and Kern R 1972 Migration brownienne de cristallites sur une surface et relation avec l'épitaxie. III. Cas de l'aluminium sur KCl; précisions sur le mécanisme de glissement *Surf. Sci.* **30** 43–52

[22] Bardotti L, Jensen P, Hoareau A, Treilleux M and Cabaud B 1995 Experimental observation of fast diffusion of large antimony clusters on graphite surfaces *Phys. Rev. Lett.* **74** 4694–7

[23] Goldby I M, Kuipers L, von Issendorff B and Palmer R E 1996 Diffusion and aggregation of size-selected silver clusters on a graphite surface *Appl. Phys. Lett.* **69** 2819–21

[24] Jensen P 1999 Growth of nanosctructures by cluster deposition: experiments and simple models *Rev. Mod. Phys.* **71** 1695–735

[25] Carrey J, Maurice J L, Petroff F and Vaurès A 2001 Growth of Au clusters on amorphous Al_2O_3: evidence of cluster mobility above a critical size *Phys. Rev. Lett.* **86** 4600–3

[26] Narhe R D, Khandkar M D, Shelke P B, Limaye A V and Beysens D A 2009 Condensation-induced jumping water drops *Phys. Rev.* E **80** 031604

[27] Reiss H 1968 Rotation and translation of islands in the growth of heteroepitaxial films *J. Appl. Phys.* **39** 5045–61

[28] Gates A D and Robins J L 1988 Cluster mobility calculations for gold nanoparticles (100)-NaCl substrates *Surf. Sci.* **194** 13–43

[29] Deltour P, Barrat J L and Jensen P 1997 Fast diffusion of a Lennard-Jones cluster on a crystalline surface *Phys. Rev. Lett.* **78** 4597–600

[30] Lewis L J, Jensen P, Combe N and Barrat J L 2000 Diffusion of gold nanoclusters on graphite *Phys. Rev.* B **61** 16084–90

[31] Jensen P, Clément A and Lewis L J 2004 Diffusion of nano-clusters on non-ideal surfaces *Physica* E **21** 71–6

[32] Steyer A, Guenoun P and Beysens D 1991 Growth of droplets on a substrate by diffusion and coalescence *Phys. Rev.* A **44** 8271–7

[33] Søndergård E, Kofman R, Cheyssac P and Stella A 1996 Production of nanostructures by self-organization of liquid Volmer–Weber films *Surf. Sci.* **364** 467–76

[34] Renaud G, Lazzari R and Leroy F 2009 Probing surface and interface morphology with grazing incidence small angle x-ray scattering *Surf. Sci. Rep.* **64** 255–380

[35] Olander J, Lazzari R, Mangili B, Goniakowski J, Renaud G and Jupille J 2007 Size- and temperature-dependent epitaxy for a strong film-substrate mismatch: the case of Pt/MgO(001) *Phys. Rev.* B **76** 075409

[36] Lazzari R, Leroy F, Renaud G and Jupille J 2007 Self-similarity during growth of the Au/TiO_2(110) model catalyst as seen by grazing incidence x-ray scattering techniques *Phys. Rev* B **76** 125412

[37] Lazzari R, Renaud G, Revenant C, Jupille J and Borenstzein Y 2009 Adhesion of growing nanoparticles at a glance: surface differential reflectivity spectroscopy and grazing incidence small angle x-ray scattering *Phys. Rev.* B **79** 125428

[38] Revenant C, Renaud G, Lazzari R and Jupille J 2009 Defect-pinned nucleation, growth, and dynamic coalescence of Ag islands on MgO(001): an *in situ* grazing-incidence small-angle x-ray scattering study *Phys. Rev.* B **79** 235424

[39] Renaud G, Ducruet M, Ulrich O and Lazzari R 2004 Apparatus for real time *in situ* quantitative studies of growing nanoparticles by grazing incidence small angle x-ray scattering and surface differential reflectance spectroscopy *Nucl. Instrum. Methods* B **222** 667–80

[40] Haas G, Menck A, Brune H, Barth J V, Venables J A and Kern K 1999 Nucleation and growth of supported clusters at defect sites: Pd/MgO(001) *Phys. Rev.* B **61** 11105–8

[41] Smith J R and Zhang W 2000 Stoichiometric interfaces of Al and Ag with Al_2O_3 *Acta Mater.* **48** 4395–403

[42] Zhang W and Smith J R 2000 Stoichiometry and adhesion of Nb/Al_2O_3 *Phys. Rev.* B **61** 16883–9

[43] Zhukovskii Y F, Kotomina E A, Herschendb B, Hermanssonb K and Jacobs P W M 2002 The adhesion properties of the Ag/Al_2O_3(0001) interface: an *ab initio* study *Surf. Sci.* **513** 343–58

[44] Feng J, Zhang W and Jiang W 2005 *Ab initio* study of Ag/Al_2O_3 and Au/Al_2O_3 *Phys. Rev.* B **72** 115423

[45] Lazzari R, Jupille J and Borensztein Y 1999 *In situ* study of a thin metal film by optical means *Appl. Surf. Sci.* **142** 451–4

[46] Lazzari R and Jupille J 2001 Silver layers on oxide surfaces: morphology and optical properties *Surf. Sci.* **482–485** 823–7

[47] Lazzari R, Roux S, Simonsen I, Jupille J, Bedeaux D and Vlieger J 2002 Multipolar optical absorptions in supported metallic particles: the case of Ag/Al_2O_3(0001) *Phys. Rev.* B **65** 235424

[48] Lazzari R and Jupille J 2005 Interfacial chemistry and wetting of metallic films on the hydroxylated α-Al_2O_3(0001) surface *Phys. Rev.* B **71** 045409

[49] Lazzari R and Jupille J 2011 Quantitative analysis of nanoparticle growth through plasmonics *Nanotechnology* **22** 445703

[50] Shalaev V M 1996 Electromagnetic properties of small-particle composites *Phys. Rep.* **272** 61–137

[51] Liebsch A 1993 Surface-plasmon dispersion and size dependence of Mie resonance: silver versus simple metals *Phys. Rev.* B **48** 11317–28

[52] Yamaguchi T, Yoshida S and Kinbara A 1974 Optical effect of the substrate on the anomalous absorption of aggregated silver films *Thin Solid Films* **21** 173–87

[53] Lazzari R, Simonsen I, Bedeaux D, Vlieger J and Jupille J 2001 Polarizability of truncated spheroidal island supported by a substrate: models and applications *Eur. Phys. J.* B **24** 267–84

[54] Lazzari R, Simonsen I and Jupille J 2003 Onset of charge localisation on coupling multipolar absorption modes in supported silver particles *Europhys. Lett.* **61** 541–6

[55] Lazzari R and Simonsen I 2002 `GranFilm`: a software for calculating thin-layer dielectric properties and Fresnel coefficients *Thin Solid Films* **419** 124–36

[56] Bedeaux D and Vlieger J 2001 *Optical Properties of Surfaces* (London: Imperial College Press)

[57] Simonsen I, Lazzari R, Jupille J and Roux S 2000 Numerical modelling of the optical response of supported metallic particles *Phys. Rev.* B **61** 7722–33

[58] Baletto F, Mottet C and Ferrando R 2000 Molecular dynamics simulations of surface diffusion and growth on silver and gold clusters *Surf. Sci.* **446** 31–45

[59] Vitos L, Ruban A V, Skriver H L and Kollár J 1998 The surface energy of metals *Surf. Sci.* **411** 186

[60] Kaischew R 1951 *Bull. Acad. Sci. Bulg. Sér. Phys.* **2** 191

[61] Henry C R 2005 Morphology of supported nanoparticles *Prog. Surf. Sci.* **80** 92–116

[62] Camacho-Flores J M, Sun L D, Saucedo-Zeni N, Weidlinger G, Hohage M and Zeppenfeld P 2008 Optical anisotropies of metal clusters supported on a birefringent substrate *Phys. Rev.* B **78** 075416

[63] Verre R, Fleischer K, Sofin R G S, McAlinden N, McGilp J F and Shvets I V 2011 *In situ* characterization of one-dimensional plasmonic Ag nanocluster arrays *Phys. Rev.* B **83** 125432

[64] Haarmans M T and Bedeaux D 1995 Optical properties of thin films up to second order in the thickness *Thin Solid Films* **258** 213–23

[65] Yu X, Duxbury P M, Jeffers G and Dubson M A 1991 Coalescence and percolation in thin metal films *Phys. Rev.* B **44** 13163–6

[66] Jeffers G, Dubson M A and Duxbury P M 1994 Island to percolation transition during growth of metal films *J. Appl. Phys.* **75** 5016–20

[67] Fanfoni M, Tomellini M and Volpe M 2001 Coalescence and impingement between islands in thin film growth: behavior of the island density kinetics *Phys. Rev.* B **64** 075409

[68] Carrey J and Maurice J L 2002 Scaling laws near percolation during three-dimensional cluster growth: a Monte Carlo study *Phys. Rev.* B **65** 205401

[69] Lazzari R, Layet J M and Jupille J 2003 Electron-energy-loss channels and plasmon confinement in supported silver particles *Phys. Rev.* B **68** 045428

[70] Van Campen D G and Hrbek J 1995 Silver on alumina: adsorption and desorption study model *J. Phys. Chem.* **99** 16389–94

[71] Venables J A 2000 *Introduction to Surface and Thin Film Processes* (Cambridge: Cambridge University Press)

[72] Heim K R, Coyle S T, Hembree G G and Venables J A 1996 Growth of nanometer-size metallic particles on CaF_2(111) *J. Appl. Phys.* **80** 1161–70

[73] Menck A 1998 Defects and growth processes at ionic and oxide crystal surfaces studied by atomic force microscopy *PhD Thesis* Ecole Polytechnique Fédérale de Lausanne

[74] Venables J A 1973 Rate equations approaches to thin film nucleation kinetics *Phil. Mag.* **27** 697–738

[75] Venables J A and Harding J H 2000 Nucleation and growth of supported metal clusters at defect sites on oxide and halide (001) surfaces *J. Cryst. Growth* **211** 27–33

[76] Zinsmeister G 1966 A contribution to Frenkel's theory of condensation *Vacuum* **16** 529–35

[77] Venables J A, Spiller G D T and Hanbücken M 1984 Nucleation and growth of thin films *Rep. Prog. Phys.* **47** 399–459

[78] Markov I 1971 The influence of surface diffusion processes on the kinetics of heterogeneous nucleation *Thin Solid Films* **8** 281–92

[79] Markov I and Kashchiev D 1972 Nucleation on active centers: general theory *J. Cryst. Growth* **16** 170–6

[80] Højrup-Hansen K, Ferrero S and Henry C R 2004 Nucleation and growth kinetics of gold nanoparticles on MgO(001) studied by UHV-AFM *Appl. Surf. Sci.* **226** 167–72

[81] Meyer R, Ge Q, Lockemeyer J, Yeates R, Lemanski M, Reinalda D and Neurock M 2007 An *ab initio* analysis of adsorption and diffusion of silver atoms on alumina surfaces *Surf. Sci.* **601** 134–45

[82] Robins J L and Rhodin T N 1964 Nucleation of metal crystals on ionic surfaces *Surf. Sci.* **2** 346–55

[83] Shedov E V, Postnikov V S and Ievlev V M 1977 Nucleus saturation density and epitaxy in the condensation of metals on alkali-halide crystals *Phys. Status Solidi* **44** 423

[84] Jensen P, Larralde H, Meunier M and Pimpinelli A 1998 Growth of three-dimensional structures by atomic deposition on surfaces containing defects: simulation and theory *Surf. Sci.* **412/413** 458–76

[85] Markov I and Kashchiev D 1972 The role of active centers in the kinetics of new phase formation *J. Cryst. Growth* **13/14** 131–4

[86] Chakraverty B K 1967 Grain size distribution in thin films-2 : non-conservative systems *J. Phys. Chem. Solids* **28** 2413–24121

[87] Henry C R and Meunier M 1998 Power laws in the growth kinetics of metal clusters on oxide substrate *Vacuum* **50** 157–63

[88] Carrey J and Maurice J L 2001 Transition from droplet growth to percolation: Monte Carlo simulations and analytical model *Phys. Rev.* B **63** 245408

[89] Vincent R 1971 A theoretical analysis and computer simulations of the growth of an epitaxial films *Proc. R. Soc.* A **321** 53–68

[90] Steyer A, Guenoun P and Beysens D 1992 Spontaneaous jumps of droplets *Phys. Rev. Lett.* **68** 64–6

[91] Ala-Nissila T, Ferrando R and Ying S C 2002 Collective and single particle diffusion on surfaces *Adv. Phys.* **51** 949–1078

[92] Bogicevic A, Liu S, Jacobsen J, Lundqvist B and Metiu H 1998 Island migration caused by the motion of the atoms at the border: size andtemperature dependence of the diffusion coefficient *Phys. Rev.* B **57** R949–R9462

[93] Mattsson T R, Mills G and Metiu H 1999 A new method for simulating the late stages of island coarsening in thin film growth: the role of island diffusion and evaporation *J. Chem. Phys.* **110** 12151–60

[94] Mills G, Mattsson T R, Møllnitz L and Metiu H 1999 Simulations of mobility and evaporation rate of adsorbate islands on solid surfaces *J. Chem. Phys.* **111** 8639–50

[95] Hamilton J C 1996 Magic size effects for heteroepitaxial islands diffusion *Phys. Rev. Lett.* **77** 885–8

[96] Hamilton J C, Sorensen M R and Voter A F 2000 Compact surface-cluster diffusion by concerted rotation and translation *Phys. Rev.* B **61** 5125–8

[97] Luedtke W D and Landman U 1999 Slip diffusion and Lévy flight of adsorbed gold nanocluster *Phys. Rev. Lett.* **82** 3835–7

[98] Brune H 1998 Microscopic view of epitaxial metal growth: nucleation and aggregation *Surf. Sci. Rep.* **31** 125–229

[99] Gates A D and Robins J L 1987 A universal model for the nucleation of gold on NaCl *Thin Solid Films* **149** 113–28

[100] Chatain D, Chabert F, Ghetta V and Fouletier J 1994 New experimental setup for wettability characterization under monitored oxygen activity : II Wettability of sapphire by silver–oxygen melts *J. Am. Ceram. Soc.* **77** 197–201

[101] Muolo M L, Valenza F, Passerone A and Passerone D 2008 Oxygen influence on ceramics wettability by liquid metals: Ag/α-Al_2O_3: experiments and modelling *Mater. Sci. Eng.* A **495** 153–8

[102] Piliar R M and Nutting J 1967 Solid–solid interfacial energy determinations in metal-ceramic systems *Phil. Mag.* **139** 181–8

[103] Tyson W R and Miller W A 1977 Surface free energies of solid metals: estimation from liquid surface tension measurements *Surf. Sci.* **62** 267

[104] Müller P and Mottet C 2007 Equilibrium nanoshapes: from thermodynamics to atomistic simulations *J. Comput. Theor. Nanosci.* **4** 316–25

[105] Prieto J E and Markov I 2010 Effect of the lattice misfit on the equilibrium shape of strained islands in the Volmer–Weber growth *Phys. Rev.* B **82** 165423

[106] Müller P and Kern R 1998 Equilibrium shape of epitaxially strained crystals (Volmer Weber case) *J. Cryst. Growth* **193** 257–70

[107] Müller P and Kern R 2000 Equilibrium nano-shape changes induced by epitaxial stress (generalised Wulff–Kaishew theorem) *Surf. Sci.* **457** 229–53

[108] Müller P and Kern R 2000 Equilibrium nano-shape change induced by epitaxial stress: effect of surface stress *Appl. Surf. Sci.* **164** 68–71

[109] Barnard A S and Zapol P 2004 A model of the phase stability of arbitrary nanoparticles as functtion of size and shape *J. Chem. Phys.* **121** 4276–83

[110] Lagarde P, Colonna S, Flank A M and Jupille J 2003 Elastic strains in silver clusters supported on MgO(100) *Surf. Sci.* **524** 102

[111] Goniakowski J and Mottet C 2005 Palladium nanoclusters on the MgO(100) surface: substrate-induced characteristicss of morphology and atomic structure *J. Cryst. Growth* **275** 29–38

[112] Mottet J, Goniakowski C, Baletto F, Ferrnando R and Treglia G 2007 Influence of epitaxial strain on supported metal cluster shapes via atomistic simulations *J. Comput. Theor. Nanosci.* **4** 326–34

[113] Goniakowski J, Jelea A, Mottet C, Barcaro G, Fortunelli A, Kuntova Z, Nita F, Levi A C, Rossi G and Ferrando R 2009 Structures of metal nanoparticles adsorbed on MgO(001): II. Pt and Pd *J. Chem. Phys.* **130** 174703

[114] Sivaramakrishnan S, Wen J, Scarpelli M E, Piercen B J and Zuo J-M 2010 Equilibrium shapes and triple line energy of epitaxial gold nanocrystals supported on TiO_2(110) *Phys. Rev.* B **82** 195421

[115] Medasani B, Park Y H and Vasiliev I 2007 Theoretical study of the surface energy, stress and lattice contraction of silver nanoparticles *Phys. Rev.* B **75** 235436

[116] Baletto F, Ferrando R, Fortunelli A, Montalenti F and Mottet C 2002 Crossover among structural motifs in transition and noble metal clusters *J. Chem. Phys.* **116** 3856–63

[117] Mottet C, Goniakowski J, Baletto F, Ferrando R and Treglia G 2004 Modeling free and supported metallic nanoclusters: structure and dynamics *Phase Transit.* **77** 101–13

[118] Ferrando R, Rossi G, Levi A C, Kuntova Z, Nita F, Jelea A, Mottet C, Barcaro G, Fortunelli A and Goniakowski J 2009 Structures of metal nanoparticles adsorbed on MgO(001). I. Ag and Au *J. Chem. Phys.* **130** 174702

[119] Wong D and Thouless M D 1997 Effects of elastic relaxation on aspect ratios during island growth of isotropic films *J. Mater. Sci.* **32** 1835–40

[120] Larsson E M, Langhammer C, Zorić I and Kasemo B 2009 Nanoplasmonic probes of catalytic reactions *Science* **326** 1091–4

[121] Bingham J M, Anker J N, Kreno L E and Van Duyne R P 2010 Gas sensing with high-resolution localized surface plasmon resonance spectroscopy *J. Am. Chem. Soc.* **132** 17358–9